Available online at www.sciencedirect.com
SCIENCE DIRECT®
Advances in Water Resources 26 (2003) 435–444
Advances in Water Resources
www.elsevier.com/locate/advwatres

Control volume function approximation methods and their applications to modeling porous media flow

Baoyan Li, Zhangxin Chen *, Guanren Huan *

Department of Mathematics, Southern Methodist University, Box 750156, Dallas, TX 75275-0156, USA

Received 27 February 2002; received in revised form 10 September 2002; accepted 15 November 2002

Abstract

In this paper we introduce a new control volume method for the discretization of a partial differential equation. The interpolation in this method utilizes 'bilinear', spline, or weighted distance functions. We call this new method the control volume function approximation (CVFA) method. It can accurately approximate both the pressure and velocity in the simulation of multiphase flow in porous media, effectively reduce grid orientation effects, and be easily applied to arbitrarily shaped control volumes. It is suitable for hybrid grid porous media simulations. In this paper we focus on its development, numerical study, and comparison with a standard control volume finite element method. A two-phase incompressible flow problem is used to show the efficiency and accuracy of the CVFA.

AMS: 35K60; 35K65; 76S05; 76T05
Keywords: Control volume function approximation; Two-phase flow; Global pressure; Porous media; Control volume finite element; Numerical experiments

1. Introduction

The finite difference method has been widely used in the numerical simulation of fluid flow in porous media. However, this method causes numerical dispersion and grid orientation problems [2,11]. It also possesses difficulties in the treatment of complicated geometry and boundary conditions. To overcome these deficiencies, one has to utilize the intrinsic grid flexibility of the finite element method [10], but this method does not conserve mass locally [8]. Recently, the control volume finite element (CVFE) method has been developed to enforce such a conservation property [12], but it often produces inaccurate fluid velocities and cannot easily generate the streamlines of fluid flow in porous medium simulations. The reason is that the usual CVFE method uses linear interpolation on each element to represent pressure, and so leads to constant interpolation for velocity.

In this paper we introduce a new control volume method for the discretization of a partial differential equation. The interpolation in this method utilizes 'bilinear', spline, or weighted distance functions, instead of polynomial functions employed in the CVFE. We call this new method the control volume function approximation (CVFA) method. This new method has a clear physical meaning in the treatment of the fluid flux in a porous media flow simulation, and can accurately approximate both this flux and the pressure. The most advantageous feature of the CVFA is that it has no requirement on the shape of control volumes. Thus it is very suitable for hybrid grid reservoir simulations. In this paper we focus on the development and numerical implementation of the CVFA and its comparison with the CVFE. The numerical study shows that the CVFA produces smaller approximation errors, has less grid orientation effects, and can handle arbitrarily shaped elements. A two-phase incompressible flow problem is used to show the efficiency and accuracy of the CVFA.

The organization of this paper is as follows. In the next section we introduce the CVFA and perform numerical tests. In the third section we apply it to two-phase incompressible flow in a porous medium. Concluding remarks are given in the last section.

* Corresponding authors.
E-mail addresses: bli@mail.smu.edu (B. Li), zchen@mail.smu.edu (Z. Chen), huan@golem.math.smu.edu (G. Huan).

0309-1708/03/$ - see front matter
doi:10.1016/S0309-1708(02)00161-6

2. The CVFA method

Throughout this paper, a two-dimensional domain Ω is considered; an extension to the three-dimensional case will be considered in future work.

2.1. Theoretical development

For the purpose of introduction, we consider the model problem

$$\begin{aligned} &-\nabla\cdot(\mathbf{a}(\mathbf{x})\nabla p) = q(\mathbf{x}), \quad \mathbf{x}\in\Omega,\\ &\mathbf{a}(\mathbf{x})\nabla p\cdot\boldsymbol{\nu} = g_N(\mathbf{x}), \quad \mathbf{x}\in\Gamma_N,\\ &p = g_D(\mathbf{x}), \quad \mathbf{x}\in\Gamma_D, \end{aligned} \tag{2.1}$$

where $\Gamma=\Gamma_N\cup\Gamma_D$ is the boundary of Ω, $\Gamma_N\cap\Gamma_D=\emptyset$, $\mathbf{a}$ is a bounded, symmetric, and positive-definite tensor, q and g_N are integrable functions on Ω and Γ_N, respectively, g_D is bounded on Γ_D, and $\boldsymbol{\nu}$ is the outer unit normal to Γ. Note that in the pure Neumann case, the solution p to (2.1) is unique up to an additive constant, and q and g_N need to satisfy the compatibility condition

$$\int_\Omega q\,\mathrm{d}\mathbf{x}+\int_\Gamma g_N\,\mathrm{d}\ell = 0.$$

A partition T_h of Ω consists of a set of (open) control volumes V_i:

$$\bar{\Omega}=\bigcup_{i=1}^{N}\bar{V}_i, \quad V_i\cap V_j=\emptyset,\ i\neq j,$$

where N is the total number of control volumes and $\bar{\Omega}$ is the closure of Ω. Different control volumes can have different shapes; see Fig. 1. They can be generated from basic triangular, quadrilateral, and/or elliptic elements; they can also stand alone as the elements of a partition of Ω. We define the boundary of each V_i by

$$\partial V_i=\bigcup_{k=1}^{N_i}e_{ik}, \tag{2.2}$$

where N_i is the number of edges e_{ik} on ∂V_i.

On each control volume V_i, we integrate the first equation of (2.1) and use the divergence theorem to see that

$$-\int_{\partial V_i}\mathbf{a}\nabla p\cdot\boldsymbol{\nu}_i\,\mathrm{d}\ell=\int_{V_i}q\,\mathrm{d}\mathbf{x}, \quad i=1,2,\ldots,N, \tag{2.3}$$

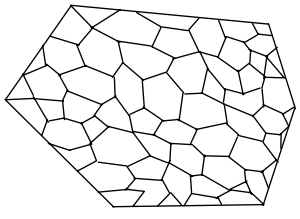

Fig. 1. A partition of Ω into control volumes.

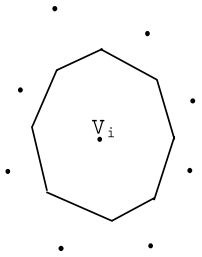

Fig. 2. A control volume.

where $\boldsymbol{\nu}_i$ is the outer unit normal to ∂V_i. On $e_{ik}\subset\partial V_i$, an interpolant p_h is used to approximate p:

$$p_h(\mathbf{x})=\sum_{j=1}^{R_{ik}}p^i_{k,j}\varphi^i_{k,j}(\mathbf{x}), \quad \mathbf{x}\in e_{ik},\ i=1,2,\ldots,N, \tag{2.4}$$

where R_{ik} is the number of interpolation nodes $\mathbf{x}^i_{k,j}$ for e_{ik} and these nodes can be located on or surrounding V_i; see Fig. 2. The basis functions $\varphi^i_{k,j}$ are defined as follows:

$$\varphi^i_{k,j}(\mathbf{x})=\begin{cases}1 & \text{at the node } \mathbf{x}^i_{k,j},\\ 0 & \text{at other nodes,}\end{cases}$$

for $j=1,2,\ldots,R_{ik}, k=1,2,\ldots,N_i$, and $i=1,2,\ldots,N$. As a result, we see that $p^i_{k,j}$ represents the pressure at the jth interpolation node $\mathbf{x}^i_{k,j}$ for e_{ik}. These basis functions are supposed to satisfy the property:

$$\begin{aligned} &\sum_{j=1}^{R_{ik}}\varphi^i_{k,j}(\mathbf{x})=1, \quad \mathbf{x}\in e_{ik},\ k=1,2,\ldots,N_i,\\ &\quad i=1,2,\ldots,N. \end{aligned} \tag{2.5}$$

This means that a constant pressure is also represented by (2.3). This property is important in the local mass conservation of the CVFA method discussed in this section. It will be also used in establishing the important relation (2.11) below.

Application of (2.2) to (2.3) yields

$$-\sum_{k=1}^{N_i}\int_{e_{ik}}\mathbf{a}\nabla p\cdot\boldsymbol{\nu}_{ik}\,\mathrm{d}\ell=\int_{V_i}q\,\mathrm{d}\mathbf{x}, \quad i=1,2,\ldots,N, \tag{2.6}$$

where $\boldsymbol{\nu}_{ik}$ is the outer unit normal to the edge e_{ik}. By substituting (2.4) into (2.6), we have

$$\begin{aligned} &-\sum_{k=1}^{N_i}\sum_{j=1}^{R_{ik}}\int_{e_{ik}}a(\mathbf{x})p^i_{k,j}\nabla\varphi^i_{k,j}(\mathbf{x})\cdot\boldsymbol{\nu}_{ik}\,\mathrm{d}l=\int_{V_i}q\,\mathrm{d}\mathbf{x},\\ &\quad i=1,2,\ldots,N. \end{aligned} \tag{2.7}$$

Set

$$T^i_{k,j}=-\int_{e_{ik}}a(\mathbf{x})\nabla\varphi^i_{k,j}(\mathbf{x})\cdot\boldsymbol{\nu}_{ik}\,\mathrm{d}l, \quad Q_i=\int_{V_i}q\,\mathrm{d}\mathbf{x}, \tag{2.8}$$

for $j=1,2,\ldots,R_{ik}$, $k=1,2,\ldots,N_i$, and $i=1,2,\ldots,N$. Then (2.7) becomes

$$\sum_{k=1}^{N_i}\sum_{j=1}^{R_{ik}}T^i_{k,j}p^i_{k,j}=Q_i, \quad i=1,2,\ldots,N. \tag{2.9}$$

This is a linear system for $p^i_{k,j}$.

We make a few remarks on the quantity $T^i_{k,j}$. First, if $e_{ik} \subset \Gamma_N$ in (2.6), then the flux on this edge is given by g_N; if $e_{ik} \subset \Gamma_D$, then the pressure in (2.7) on this edge is given by g_D. A Robin boundary condition (third or mixed type) can also be easily incorporated into (2.6). Second, $T^i_{k,j}$ is usually calculated with numerical integration (quadrature rules). Third, if $\mathbf{a}$ is a scalar a and different on the two sides of an edge of V_i, across that edge it can be approximated by the harmonic average

$$a(\mathbf{x}) = \frac{2a_i^+(\mathbf{x})a_i^-(\mathbf{x})}{a_i^+(\mathbf{x}) + a_i^-(\mathbf{x})}, \tag{2.10}$$

where a_i^+ and a_i^- indicate the values from the two sides. If $\mathbf{a}$ is a tensor, this harmonic average can be used for each component of $\mathbf{a}$. The reason for using a harmonic average is that for an inactive point (i.e., the point where $a = 0$), this average will give the same value (i.e., $a = 0$). Fourth, the standard upstream technique can be exploited in the computation of $T^i_{k,j}$. Also, if a control volume V_i contains a well (see the next section for a flow problem), the upstream weighting technique should be employed for Q_i as well. Finally, $T^i_{k,j}$ satisfies the property

$$\sum_{j=1}^{R_{ik}} T^i_{k,j} = 0, \quad k = 1, 2, \ldots, N_i, \ i = 1, 2, \ldots, N. \tag{2.11}$$

This can be easily seen from (2.5). It now remains to construct the basis functions $\varphi^i_{k,j}$. Below we will construct three kinds of basis functions.

2.1.1. '*Bilinear*' *function approximation*

The interpolation nodes in the approach of this subsection are the centers of control volumes. Consider an edge e_{i1} of a control volume V_i with center $\mathbf{x}_i$. The value of p at any point $\mathbf{x}$ on e_{i1} can be obtained by its values at the nodes $\mathbf{x}_i, \mathbf{x}^i_1, \mathbf{x}^i_2$, and $\mathbf{x}^i_3$, as shown in Fig. 3. The three latter nodes are the centers of the control volumes adjacent to V_i. Introduce points $\mathbf{x}^i_{1i}$ and $\mathbf{x}^i_{23}$ which lie on the line segments $\mathbf{x}^i_1\mathbf{x}_i$ and $\mathbf{x}^i_2\mathbf{x}^i_3$, respectively, and satisfy

$$\frac{|\mathbf{x}^i_1 - \mathbf{x}^i_{1i}|}{|\mathbf{x}_i - \mathbf{x}^i_{1i}|} = \frac{|\mathbf{x}^i_2 - \mathbf{x}^i_{23}|}{|\mathbf{x}^i_3 - \mathbf{x}^i_{23}|},$$

where $|\cdot|$ indicates the distance. The values at $\mathbf{x}^i_{1i}$ and $\mathbf{x}^i_{23}$ are obtained by 'linear' interpolation:

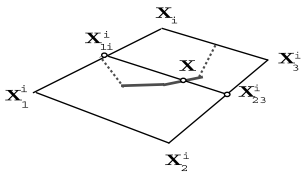

Fig. 3. A bilinear approximation.

$$p^i(\mathbf{x}^i_{1i}) = p^i(\mathbf{x}^i_1) + \frac{|\mathbf{x}^i_{1i} - \mathbf{x}^i_1|}{|\mathbf{x}_i - \mathbf{x}^i_1|}\left(p^i(\mathbf{x}_i) - p^i(\mathbf{x}^i_1)\right),$$

$$p^i(\mathbf{x}^i_{23}) = p^i(\mathbf{x}^i_2) + \frac{|\mathbf{x}^i_{23} - \mathbf{x}^i_2|}{|\mathbf{x}^i_3 - \mathbf{x}^i_2|}\left(p^i(\mathbf{x}^i_3) - p^i(\mathbf{x}^i_2)\right).$$

Now, applying 'linear' interpolation again, the value of p at $\mathbf{x}$ is found by

$$\begin{aligned} p^i(\mathbf{x}) &= p^i(\mathbf{x}^i_{1i}) + \frac{|\mathbf{x} - \mathbf{x}^i_{1i}|}{|\mathbf{x}^i_{23} - \mathbf{x}^i_{1i}|}\left(p^i(\mathbf{x}^i_{23}) - p^i(\mathbf{x}^i_{1i})\right) \\ &= \sum_{k=0}^{3} \varphi^i_{1,k} p^i_k, \end{aligned} \tag{2.12}$$

where $p^i_0 = p^i(\mathbf{x}_i)$ and

$$\varphi^i_{0,1} = \frac{|\mathbf{x}^i_{1i} - \mathbf{x}^i_1|}{|\mathbf{x}_i - \mathbf{x}^i_1|}\left(1 - \frac{|\mathbf{x} - \mathbf{x}^i_{1i}|}{|\mathbf{x}^i_{23} - \mathbf{x}^i_{1i}|}\right),$$

$$\varphi^i_{1,1} = \left(1 - \frac{|\mathbf{x}^i_{1i} - \mathbf{x}^i_1|}{|\mathbf{x}_i - \mathbf{x}^i_1|}\right)\left(1 - \frac{|\mathbf{x} - \mathbf{x}^i_{1i}|}{|\mathbf{x}^i_{23} - \mathbf{x}^i_{1i}|}\right),$$

$$\varphi^i_{2,1} = \left(1 - \frac{|\mathbf{x}^i_{23} - \mathbf{x}^i_2|}{|\mathbf{x}^i_3 - \mathbf{x}^i_2|}\right)\frac{|\mathbf{x} - \mathbf{x}^i_{1i}|}{|\mathbf{x}^i_{23} - \mathbf{x}^i_{1i}|},$$

$$\varphi^i_{3,1} = \frac{|\mathbf{x}^i_{23} - \mathbf{x}^i_2|}{|\mathbf{x}^i_3 - \mathbf{x}^i_2|}\,\frac{|\mathbf{x} - \mathbf{x}^i_{1i}|}{|\mathbf{x}^i_{23} - \mathbf{x}^i_{1i}|}.$$

Representation (2.12) can be extended to other edges e_{ij} of V_i:

$$p^i(\mathbf{x}) = \sum_{k=0}^{3} \varphi^i_{k,j} p^i_{k+j-1}.$$

Note that these functions are defined in terms of distances and look like bilinear functions in form. That is why we have quoted 'bilinear'.

We point out a difference between the 'bilinear' function approximation in the CVFA and the linear polynomial approximation in the CVFE. The latter method is based on control volumes which are generated from triangles. Let points $0, 1, \ldots, 5$ be vertices of triangles (see Fig. 4). They are the centers of control volumes. In the CVFE [12,17], the velocity vector $\mathbf{u} = -\mathbf{a}(\mathbf{x})\nabla p$ at the interface ac is calculated by linear polynomial interpolation which involves the values of p at points 0, 1 and 2. In fact, the calculation of $\mathbf{u}$ at all

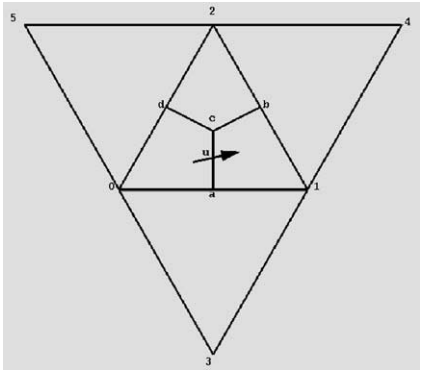

Fig. 4. Interpolation points for the CVFA.

interfaces ac, bc, and dc in the CVFE involves only points 0, 1 and 2. In contrast, in the CVFA the calculation of $\mathbf{u}$ at ac from the above construction involves the values of p at points 0, 1, 2 and 3. Similarly, the calculation of $\mathbf{u}$ at bc and dc involves 0, 1, 2 and 4, and 0, 1, 2 and 5, respectively. In this manner, the fluxes on the interfaces between control volumes are guaranteed to be continuous. Also, since the CVFA uses higher order interpolation, the calculation of $\mathbf{u}$ is more accurate than that in the CVFE.

2.1.2. Spline function approximation

It is well known that spline functions have good smoothness properties and have been used in many areas [16]. Here we utilize them to define our interpolation functions. First, we define

$$\omega^i_{k,j}(\mathbf{x}) = a^i_{k,j} + b^i_{k,j}x_1 + c^i_{k,j}x_2 + \sum_{l=1}^{R_{ik}} f^i_{k,j,l} h^i_{k,j,l}(\mathbf{x}),$$
$$\mathbf{x} = (x_1, x_2) \in e_{ik}, \tag{2.13}$$

where $a^i_{k,j}, b^i_{k,j}, c^i_{k,j}, f^i_{k,j,l} \in \Re$, and

$$h^i_{k,j,l}(\mathbf{x}) = 2(r^i_{k,j,l})^2 \ln r^i_{k,j,l},$$
$$r^i_{k,j,l}(x_1, x_2) = ((x_1 - x^i_{1,k,l})^2 + (x_2 - x^i_{2,k,l})^2)^{1/2},$$

with $\mathbf{x}^i_{k,l} = (x^i_{1,k,l}, x^i_{2,k,l})$ being the node coordinates, $j,\ l = 1, 2, \ldots, R_{ik},\ i = 1, \ldots, N$. These spline functions are required to satisfy these properties:

- nodal values:
$$\omega^i_{k,j}(\mathbf{x}) = \begin{cases} 1 & \text{at the node } \mathbf{x}^i_{k,j}, \\ 0 & \text{at other nodes,} \end{cases}$$
- zero total force:
$$\sum_{l=1}^{R_{ik}} f^i_{k,j,l} = 0,$$
- and zero total force moment:
$$\sum_{l=1}^{R_{ik}} f^i_{k,j,l} \mathbf{x}^i_{k,l} = 0.$$

It can be checked that these three constraints can be used to determine the coefficients $a^i_{k,j}, b^i_{k,j}, c^i_{k,j}$, and $f^i_{k,j,l}$ with an appropriate choice of the interpolation nodes $\mathbf{x}^i_{k,j}$. In general, these nodes are the centers of control volumes. For the simplest spline approach, we can use four neighboring nodes to interpolate p and $\mathbf{u}$, as in Section 2.1.1. For higher order interpolation, we use more nodes.

Now, the basis functions $\varphi^i_{k,j}$ are expressed as

$$\varphi^i_{k,j}(\mathbf{x}) = \frac{\omega^i_{k,j}(\mathbf{x})}{\sum_{l=1}^{R_{ik}} \omega^i_{k,l}(\mathbf{x})}, \quad \mathbf{x} \in e_{ik}.$$

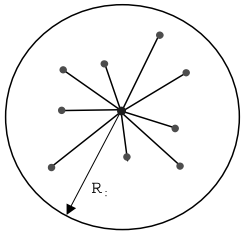

Fig. 5. A distance weighted approximation.

Since there is no limit on the shape of control volumes, this approach is suitable for unstructured grid reservoir simulations.

2.1.3. Distance weighted approximation

We now introduce a simple approach to construct basis functions. This approach appears the most flexible on the choice of the shape of control volumes. To each control volume V_i, we associate with a circle of radius R_i which encloses the nodes $\mathbf{x}^i_{k,j}, j = 1, 2, \ldots, R_{ik}$. In general, this circle is centered at the center of gravity of V_i. For each node $\mathbf{x}^i_{k,j}$, we define the distance function (see Fig. 5).

$$r^i_{k,j}(\mathbf{x}) = |\mathbf{x} - \mathbf{x}^i_{k,j}|, \quad \mathbf{x} \in e_{ik}, \quad j = 1, 2, \ldots, R_{ik},$$
$$k = 1, 2, \ldots, N_i, \quad i = 1, 2, \ldots, N.$$

We now define the basis functions $\varphi^i_{k,j}$ by

$$\varphi^i_{k,j}(\mathbf{x}) = \begin{cases} \frac{w^i_{k,j}(\mathbf{x})}{w^i_k(\mathbf{x})} & \text{for } \mathbf{x} \neq \mathbf{x}^i_{k,j}, \\ 1 & \text{for } \mathbf{x} = \mathbf{x}^i_{k,j}, \end{cases}$$

where

$$w^i_{k,j}(\mathbf{x}) = \left(1 - \frac{R_i}{r^i_{k,j}(\mathbf{x})}\right)^{\epsilon}, \quad w^i_k(\mathbf{x}) = \sum_{j=1}^{R_{ik}} w^i_{k,j}(\mathbf{x}), \quad \epsilon > 0.$$

Again, thanks to the use of distance functions, the definition of these basis functions does not have a specific requirement on the shape of control volumes, and the nodes can be the centers of control volumes.

2.2. Numerical example I

We first numerically check convergence rates of the CVFA. To compare with the CVFE, the control volumes used are generated from triangles, as noted earlier. In (2.1), let $\Omega = (0,1) \times (0,1)$ be the unit square, $\mathbf{a}$ be the identity tensor, and

$$q(\mathbf{x}) = 2\pi^2 \cos(\pi x_1) \cos(\pi x_2).$$

The boundary condition is

$$\nabla p \cdot \boldsymbol{\nu} = 0, \quad x_1 = 0 \text{ and } x_1 = 1,\ x_2 \in (0,1),$$
$$p = \cos(\pi x_1), \quad x_2 = 0,\ x_1 \in (0,1),$$
$$p = -\cos(\pi x_1), \quad x_2 = 1,\ x_1 \in (0,1).$$

Table 1
Numerical results for p in the CVFA

$1/h$	$\|p-p_h\|_{L^\infty(\Omega)}$	Rate	$\|p-p_h\|_{L^2(\Omega)}$	Rate
2	0.31147353	–	0.18388206	–
4	0.11490560	1.4387	4.8526985E−02	1.9219
8	3.2336764E−02	1.8292	1.2107453E−02	2.0029
16	8.3515844E−03	1.9531	3.0019570E−03	2.0199
32	2.1060989E−03	1.9875	7.4598770E−04	2.0087
64	5.2769621E−04	1.9968	1.8585293E−04	2.0050

Table 2
Numerical results for $\mathbf{u}$ in the CVFA

$1/h$	$\|\mathbf{u}-\mathbf{u}_h\|_{L^\infty(\Omega)}$	Rate	$\|\mathbf{u}-\mathbf{u}_h\|_{L^2(\Omega)}$	Rate
2	1.35576698	–	1.00055733	–
4	0.79144271	0.7766	0.40574242	1.3022
8	0.41524124	0.9305	0.15380230	1.3995
16	0.21064551	0.9791	6.3754123E−02	1.2705
32	0.10577494	0.9938	2.8906865E−02	1.1411
64	5.2954964E−02	0.9982	1.3795696E−02	1.0672

Table 3
Numerical results for p in the CVFE

$1/h$	$\|p-p_h\|_{L^\infty(\Omega)}$	Rate	$\|p-p_h\|_{L^2(\Omega)}$	Rate
2	0.35502877	–	0.18584850	–
4	0.11549486	1.6201	5.8970002E−02	1.6561
8	3.3079427E−02	1.8038	1.5744807E−02	1.9051
16	8.7789616E−03	1.9138	4.0029721E−03	1.9757
32	2.2525012E−03	1.9625	1.0049860E−03	1.9939
64	5.6991337E−04	1.9827	2.5151431E−04	1.9985

Table 4
Numerical results for $\mathbf{u}$ in the CVFE

$1/h$	$\|\mathbf{u}-\mathbf{u}_h\|_{L^\infty(\Omega)}$	Rate	$\|\mathbf{u}-\mathbf{u}_h\|_{L^2(\Omega)}$	Rate
2	1.8475225	–	1.2560773	–
4	1.3093706	0.4967	0.68846096	0.8675
8	0.70851284	0.8860	0.35305205	0.9635
16	0.36116394	0.9721	0.17767979	0.9906
32	0.18145106	0.9931	8.8985854E−02	0.9976
64	9.0834342E−02	0.9983	4.4511228E−02	0.9994

Then the exact solution to (2.1) is $p = \cos(\pi x_1)\cos(\pi x_2)$. We have also experimented with other examples, and results similar to those presented have been observed.

Two types of norms are used to check the convergence rates:

$$\|v\|_{L^\infty(\Omega)} = \max_{\mathbf{x}\in\Omega} |v(\mathbf{x})|, \quad \|v\|_{L^2(\Omega)} = \left(\int_\Omega |v(\mathbf{x})|^2 \, d\mathbf{x} \right)^2.$$

The spline function approximation approach in Section 2.1.2 is used in the CVFA, and the interpolation nodes consist of the centers of control volumes. We use the simplest spline approach (Section 2.1.2) to compare with the CVFE. The numerical errors and the corresponding convergence rates for p and its gradient $\mathbf{u} = \nabla p$ are shown in Tables 1–4 for the CVFA and CVFE, where p_h and $\mathbf{u}_h$ are the approximate solutions of p and $\mathbf{u}$, respectively, h is the space step size in the x- and y-directions for the base triangulation, and the rate is the convergence rate in the corresponding norm. From these computational results, we see that the convergence rates for p and $\mathbf{u}$ are asymptotically of order $\mathcal{O}(h^2)$ and $\mathcal{O}(h)$ for both the CVFA and CVFE. However, from this and other numerical experiments (not reported here) we have observed that the approximation errors in the CVFA are smaller than those in the CVFE.

2.3. Numerical example II

We now consider an example which the CVFE cannot easily handle:

$$\begin{aligned} &-\Delta p = \delta(\mathbf{x}-\mathbf{x}_0), \quad \mathbf{x}\in\Omega, \\ &p = 0, \quad \mathbf{x}\in\Gamma, \end{aligned} \tag{2.14}$$

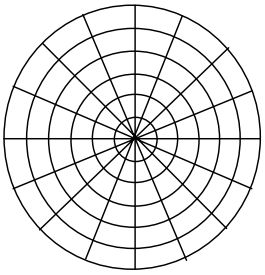

Fig. 6. A circular grid.

Table 5
Numerical results for the CVFA for test II

(N_r, N_θ)	$\|p - p_h\|_{L^2(\Omega)}$	Rate
(8,12)	4.13287534E−03	–
(16,24)	2.88767285E−03	0.5172
(32,48)	1.49421476E−03	0.9595
(64,96)	7.51098130E−04	0.9923

where $\Omega = \{\mathbf{x} \in \Re^2 : |\mathbf{x}| \leq 1\}$ is the unit circle and $\delta(\mathbf{x} - \mathbf{x}_0)$ is the Dirac delta function with center $\mathbf{x}_0$. The exact solution of (2.14) is Green's function

$$p(\mathbf{x}) = \frac{1}{2\pi} \ln\left(\frac{|\mathbf{x} - \mathbf{x}_0|}{|\mathbf{x}_0||\mathbf{x} - \mathbf{x}_0^*|}\right), \tag{2.15}$$

where $\mathbf{x}_0^*$ is the image of $\mathbf{x}_0$ with respect to Γ:

$$\mathbf{x}_0^* = \frac{1}{|\mathbf{x}_0|^2}\mathbf{x}_0.$$

For this problem, circular grids (Fig. 6) are the most appropriate. However, as noted, the CVFE cannot easily and accurately treat this type of grid. The flexibility of the CVFA on the shape of elements enables us to employ them. The numerical errors $\|p - p_h\|_{L^2(\Omega)}$ and the corresponding convergence rates for the CVFA bilinear function approach are presented in Table 5, where the uniform refinement in the radial and angular directions is measured by $h_r = 1/N_r$ and $h_\theta = 2\pi/N_\theta$, and $\mathbf{x}_0 = 0.5e^{\pi i/6}$. From this table, we see that the convergence rate in this norm is asymptotically of order $\mathcal{O}(h)$. The reduction in the rate is due to the reduction in the regularity of the solution to (2.14) (see (2.15)). Because of the nature of the solution (2.15), we are not able to use the $\|\cdot\|_{L^\infty(\Omega)}$-norm.

3. Application to two-phase flow in porous media

In this section we apply the CVFA in the previous section to two-phase flow in porous media. The model presented is for the general multi-dimensional case.

3.1. The two-phase model

For the flow of two incompressible, immiscible fluids in a porous medium $\Omega \subset \Re^d (d \leq 3)$, the mass balance equation for each of the fluid phases is [3,14]

$$\phi \frac{\partial(\rho_\alpha s_\alpha)}{\partial t} + \nabla \cdot (\rho_\alpha \mathbf{u}_\alpha) = \rho_\alpha q_\alpha, \quad \alpha = \mathrm{w}, \mathrm{o}, \tag{3.1}$$

where $\alpha = w$ denotes the wetting phase (e.g., water), $\alpha = \mathrm{o}$ indicates the nonwetting phase (e.g., oil), ϕ is the porosity of the medium, and $\rho_\alpha, s_\alpha, \mathbf{u}_\alpha$, and q_α are, respectively, the density, saturation, volumetric velocity, and external volumetric flow rate of the α-phase. The volumetric velocity $\mathbf{u}_\alpha$ is given by Darcy's law

$$\mathbf{u}_\alpha = -\frac{\kappa \kappa_{r\alpha}}{\mu_\alpha} \nabla(p_\alpha - \rho_\alpha g Z), \quad \alpha = \mathrm{w}, \mathrm{o}, \tag{3.2}$$

where κ is the absolute permeability of the porous medium, p_α, μ_α, and $\kappa_{r\alpha}$ are the pressure, viscosity, and relative permeability of the α-phase, respectively, g denotes the gravitational constant, Z is the depth, and the z-coordinate is in the vertical downward direction. In addition to (3.1) and (3.2), the customary property for the saturations is

$$s_\mathrm{w} + s_\mathrm{o} = 1, \tag{3.3}$$

and the two phase pressures are related by the capillary pressure function

$$p_\mathrm{c}(\mathbf{x}, s_\mathrm{w}) = p_\mathrm{o} - p_\mathrm{w}. \tag{3.4}$$

Finally, we define q_α in (3.1) by

$$q_\alpha = \sum_l q_\alpha^{(l)} \delta(\mathbf{x} - \mathbf{x}^{(l)}), \quad \alpha = \mathrm{w}, \mathrm{o},$$

where $q_\alpha^{(l)}$ indicates the volume of the fluid produced or injected per unit time at the lth well, $\mathbf{x}^{(l)}$, for phase α and δ is the Dirac delta function. Following [15], $q_\alpha^{(l)}$ can be defined by

$$q_\alpha^{(l)} = \frac{2\pi\kappa\kappa_{r\alpha}\Delta L^{(l)}}{\mu_\alpha \ln(r_\mathrm{e}^{(l)}/r_\mathrm{c}^{(l)})}(p^{(l)} - p_\alpha - \rho_\alpha g(Z^{(l)} - Z)), \tag{3.5}$$

where $\Delta L^{(l)}$ is the length of the lth well, $p^{(l)}$ is the flowing bottom hole pressure at the (datum level) depth $Z^{(l)}, r_\mathrm{e}^{(l)}$ is the equivalent radius, and $r_\mathrm{c}^{(l)}$ is the radius of the lth well.

In this paper Eqs. (3.1)–(3.5) are solved in an improved implicit pressure-explicit saturation (IMPES) manner. To separate the pressure and saturation equations, we introduce the phase mobility functions

$$\lambda_\alpha(\mathbf{x}, s_\alpha) = \kappa_{r\alpha}(\mathbf{x}, s_\alpha)/\mu_\alpha, \quad \alpha = \mathrm{w}, \mathrm{o},$$

and the total mobility

$$\lambda(\mathbf{x}, s) = \lambda_\mathrm{w} + \lambda_\mathrm{o},$$

where $s = s_\mathrm{w} = 1 - s_\mathrm{o}$. The fractional flow functions are defined by

$$f_\alpha(\mathbf{x}, s) = \lambda_\alpha/\lambda, \quad \alpha = \mathrm{w}, \mathrm{o}.$$

Following [1,4], we define the global pressure as

$$p = p_o - \int^s \left(f_w \frac{\partial p_c}{\partial s} \right)(\mathbf{x}, \xi)\, d\xi. \tag{3.6}$$

Finally, we define the total velocity

$$\mathbf{u} = \mathbf{u}_w + \mathbf{u}_o. \tag{3.7}$$

Now, under the assumption that the fluids are incompressible we apply (3.3) and (3.7) to (3.1) to see that

$$\nabla \cdot \mathbf{u} = q(p, s) \equiv q_w + q_o, \tag{3.8}$$

and (3.4), (3.6), and (3.7) to (3.2) to obtain

$$\mathbf{u} = -\kappa(\lambda(s)\nabla p + \gamma_1(s)), \tag{3.9}$$

where

$$\gamma_1 = -\lambda_w \nabla_{\mathbf{x}} p_c + \lambda \int^s \nabla_{\mathbf{x}} \left(f_w \frac{\partial p_c}{\partial s} \right)(\mathbf{x}, \xi)\, d\xi - (\lambda_w \rho_w + \lambda_o \rho_o) g \nabla Z.$$

Similarly, apply (3.4), (3.6), (3.9), and the constant densities to (3.1) and (3.2) with $\alpha = w$ to obtain

$$\phi \frac{\partial s}{\partial t} + \nabla \cdot \left\{ \kappa f_w(s) \lambda_o(s) \left(\frac{\partial p_c}{\partial s} \nabla s + \gamma_2(s) \right) + f_w(s)\mathbf{u} \right\} = q_w(p, s), \tag{3.10}$$

where

$$\gamma_2 = \nabla_{\mathbf{x}} p_c - (\rho_o - \rho_w) g \nabla Z.$$

In (3.8) and (3.10), the well terms are now defined in terms of the global pressure p and saturation s:

$$q_\alpha^{(l)}(p, s) = \frac{2\pi\kappa\kappa_{r\alpha}\Delta L^{(l)}}{\mu_\alpha \ln(r_e^{(l)}/r_c^{(l)})}(p^{(l)} - p - \gamma_\alpha - \rho_\alpha g(Z^{(l)} - Z)), \tag{3.11}$$

where

$$\gamma_o = \int^s \left(f_w \frac{\partial p_c}{\partial s} \right)(\mathbf{x}, \xi)\, d\xi,$$

$$\gamma_w = \int^s \left(f_w \frac{\partial p_c}{\partial s} \right)(\mathbf{x}, \xi)\, d\xi - p_c.$$

The pressure equation is given by (3.8) and (3.9), while the saturation equation is described by (3.10). They determine the main unknowns $p, \mathbf{u}$, and s. The model is completed by specifying boundary and initial conditions. In this paper we consider no flow boundary conditions

$$\mathbf{u} \cdot \boldsymbol{\nu} = 0, \quad \mathbf{x} \in \Gamma,$$
$$\left\{ \kappa f_w(s) \lambda_o(s) \left(\frac{\partial p_c}{\partial s} \nabla s + \gamma_2(s) \right) + f_w(s)\mathbf{u} \right\} \cdot \boldsymbol{\nu} = 0, \quad \mathbf{x} \in \Gamma. \tag{3.12}$$

The initial condition is given by

$$s(\mathbf{x}, 0) = s_0(\mathbf{x}), \quad \mathbf{x} \in \Omega. \tag{3.13}$$

The differential system has a clear structure; the pressure equation is elliptic for p and the saturation equation is parabolic for s. The parabolic equation is degenerate in the sense that the capillary diffusion coefficient can be zero. These two equations are nonlinear. The mathematical properties of this system such as existence, uniqueness, regularity, and asymptotic behavior of solutions have been studied in [5,6].

We end this section with two remarks. First, the global pressure p in (3.6) is used. The use of this variable reduces the coupling between pressure and saturation equations [7]. It is also convenient in the treatment of wells, as in (3.11). Second, in the case where f_w and p_c depend only on s, it follows from (3.4) and (3.6) that

$$\lambda \nabla p = \lambda_w \nabla p_w + \lambda_o \nabla p_o.$$

This implies that the global pressure is the pressure that would produce the flow of a fluid (with mobility λ) equal to the sum of the flows of fluids w and o.

3.2. The discretization

It follows from (3.8) and (3.9) that

$$-\nabla \cdot [\kappa(\lambda(s)\nabla p + \gamma_1(s))] = q(p, s).$$

This pressure equation is solved implicitly:

$$-\nabla \cdot [\kappa^n(\lambda(s^n)\nabla p^n + \gamma_1(s^n))] = q(p^n, s^n), \tag{3.14}$$

where p^n represents the value of p at time level t^n. On each control volume V_i, as in (2.3) we have

$$-\int_{\partial V_i} \kappa^n(\lambda(s^n)\nabla p^n + \gamma_1(s^n)) \cdot \boldsymbol{\nu}_i\, d\ell = \int_{V_i} q(p^n, s^n)\, d\mathbf{x}, \quad i = 1, 2, \ldots, N, \tag{3.15}$$

to which the CVFA in Section 2.1 can apply.

The saturation Eq. (3.10) is solved explicitly in time:

$$\phi \frac{s^{n+1} - s^n}{\Delta t^{n+1}} + \nabla \cdot \left\{ \kappa^n f_w(s^n) \lambda_o(s^n) \left(\frac{\partial p_c^n}{\partial s} \nabla s^n + \gamma_2(s^n) \right) + f_w(s^n)\mathbf{u}^n \right\} = q_w(p^n, s^n),$$

where Δt^{n+1} is the time step at level t^{n+1} and

$$\mathbf{u}^n = -\kappa^n(\lambda(s^n)\nabla p^n + \gamma_1(s^n)).$$

Again, as in (2.3) we see that, for $i = 1, 2, \ldots, N$,

$$\int_{V_i} \phi \frac{s^{n+1} - s^n}{\Delta t^{n+1}}\, d\mathbf{x} + \int_{\partial V_i} \left\{ \kappa^n f_w(s^n) \lambda_o(s^n) \times \left(\frac{\partial p_c^n}{\partial s} \nabla s^n + \gamma_2(s^n) \right) + f_w(s^n)\mathbf{u}^n \right\} \cdot \boldsymbol{\nu}_i\, d\ell = \int_{V_i} q_w(p^n, s^n)\, d\mathbf{x}. \tag{3.16}$$

An improved IMPES procedure [9] is used to solve (3.15) and (3.16). This procedure utilizes an adaptive control strategy on the choice of the time step for the saturation and takes a much larger time step for the pressure than for the saturation. Through a stability analysis and a comparison with a simultaneous solution procedure, we have shown that this improved procedure is effective and efficient for the numerical simulation of

Table 6
Relative permeability data

s	κ_{rw}	κ_{ro}
0.22	0	1
0.3	0.07	0.4
0.4	0.15	0.125
0.5	0.24	0.0649
0.6	0.33	0.0048
0.8	0.65	0
0.9	0.83	0
1	1	0

two-phase flow and it is capable of solving two-phase coning problems [9].

3.3. Numerical example III

This test is chosen to check the applicability of the CVFA to two-phase (water and oil) flow in a heterogeneous porous medium. The absolute permeability κ of this heterogeneous medium is randomly chosen. The porosity is $\phi = 0.2$, and the reservoir dimensions are $1000 \times 1000 \times 100$ ft^3 (the flow is two-dimensional; i.e., it is uniform in the z-direction and the gravity is ignored). There are 25 wells in this model: 13 injection and 12 production wells (see the location of wells in Fig. 9). The bottom hole pressures at injection and production wells are 3700 and 3500 psi, and the water and oil viscosities are 0.4 and 6.0 cp, respectively. The relative permeability data are given in Table 6 and the capillary pressure is zero. Piecewise linear interpolation is used for the permeabilities. No flow boundary conditions are used in this example, as in (3.12).

Since the CVFA method has no requirement on the shape of elements, we use the present two-phase flow model to show the validity of this method for rectangular grids by comparing it with the standard control volume finite difference (based on the five point stencil) method (CVFD). Fig. 7 presents the oil and water production rates Q_o and Q_w (versus time in days) calculated by the CVFA method using the 'bilinear' function and distance weighted (with the power factor $\epsilon = 1.08$) approximation approaches and the CVFD method, where CVFA-wd, CVFA-bl, and CVFD-5 indicate the CVFA-distance weighted, CVFA-bilinear function, and CVFD-five point approaches, respectively. The choice of ϵ depends on the underlying differential problem and is empirical. The grid size is chosen to be 50 ft between the centers of two control volumes, the choice of time steps is given as in [9], and the initial condition is $s_0 = 0.2$. The corresponding water cut F_w and oil recovery rate V_o are displayed in Fig. 8, where $F_w = Q_w/(Q_w + Q_o)$. From these figures we see that the numerical results from different methods match very well. As an illustration, the saturation distribution by the CVFA method with the bilinear function approximation is shown in Fig. 9.

3.4. Numerical example IV

This test uses a homogeneous model to see the grid orientation effect of the CVFA. The absolute permeability κ is 100 md. Other data are the same as those for the first flow model except the dimensions of the porous medium and the well schemes. Two cases are designed for this test. For case one, the dimensions are $1050 \times 866 \times 100$ ft^3, and there are five wells: one injection located at the center (525.00 ft, 433.00 ft) and four production wells located at (75.00 ft, 779.42 ft), (975.00 ft, 779.42 ft), (75.00 ft, 86.60 ft), and (975.00 ft, 86.60 ft). For case two, the dimensions are $1050 \times 1050 \times 100$ ft^3, the location of the injection well is (525.00 ft, 525.00 ft) (the center), and the four production wells are located at (25.00 ft, 1025.00 ft), (1025.00 ft, 1025.00 ft), (25.00 ft, 25.00 ft), and (1025.00 ft, 25.00 ft).

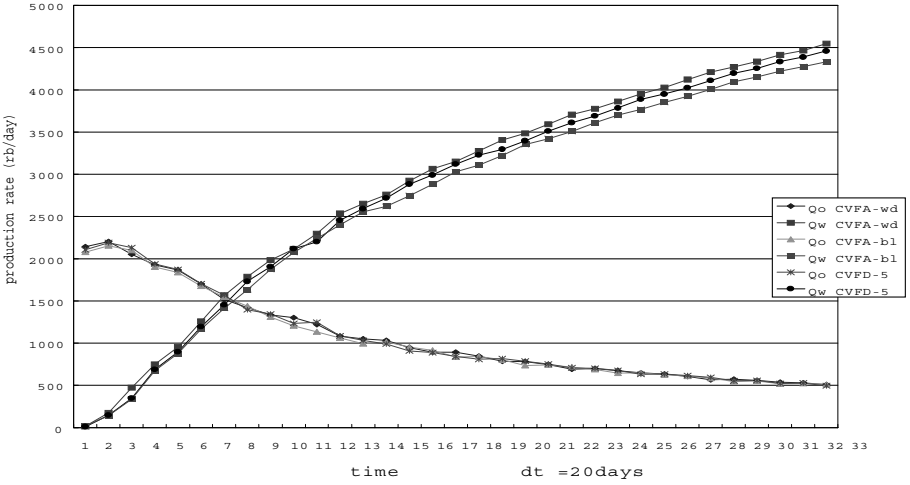

Fig. 7. Oil and water production rates Q_o and Q_w.

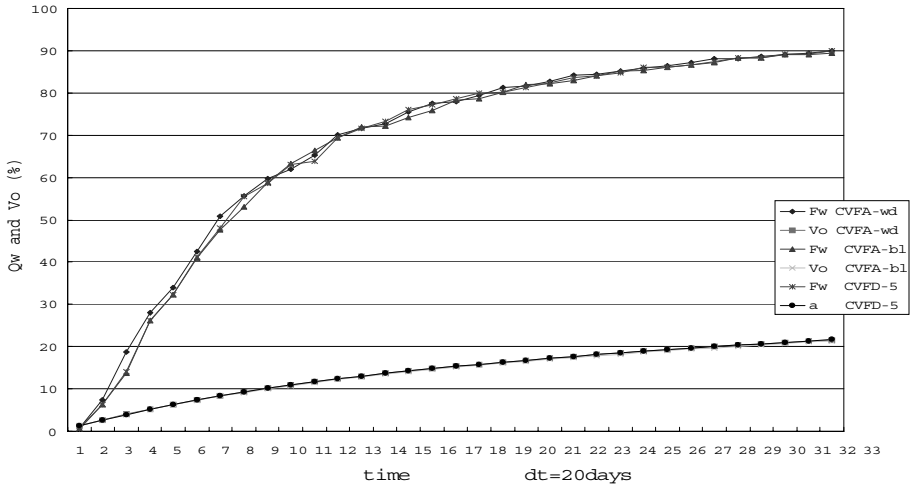

Fig. 8. Water cut F_w and oil recovery rate V_o for model one.

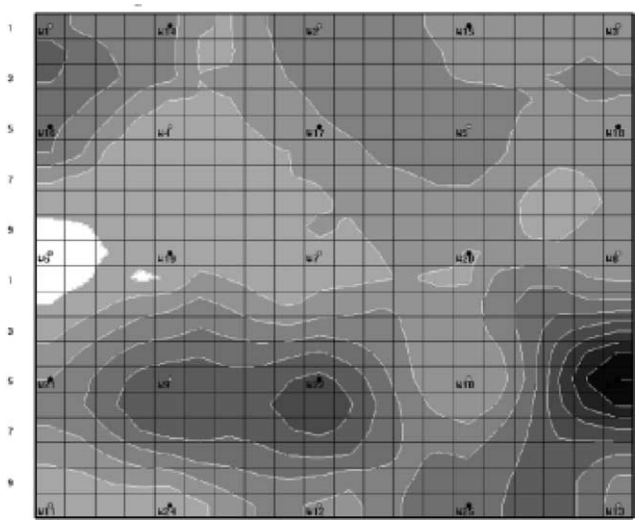

Fig. 9. Saturation distribution computed by the CVFA.

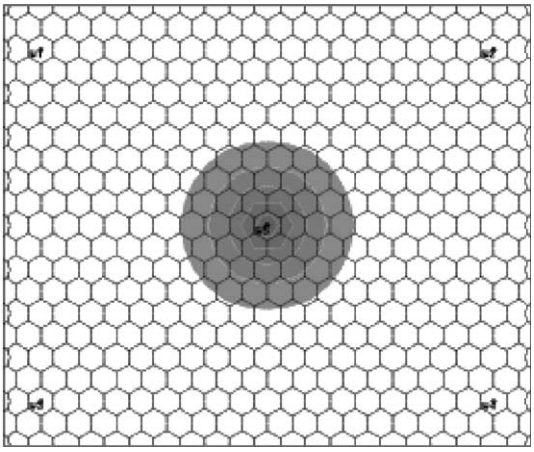

Fig. 10. The saturation of case one by the CVFA.

It can be seen that the four production wells are the same distance from the injection well in both cases.

We use the saturation profiles and water break-through times to check the grid orientation effects. The control volumes for case one are based on the Voronoi grid [13] (Fig. 10), while the control volumes for case two are generated from a triangular grid (Fig. 11). Both the CVFA and CVFE methods are applied to the two cases. Figs. 10 and 11 show the saturation profiles by the CVFA. From Fig. 10, we see that the water front is a circle for this grid system. This implies that water spreads in the same speed in all directions, and thus the Voronoi grid does not have an orientation effect. Fig. 11 shows that the front is not a circle; in particular, it has a preference to certain directions. Hence flow in the second grid system is sensitive to the grid orientation. These phenomena can also be seen from Table 7. For case one, the water break-through times of all production

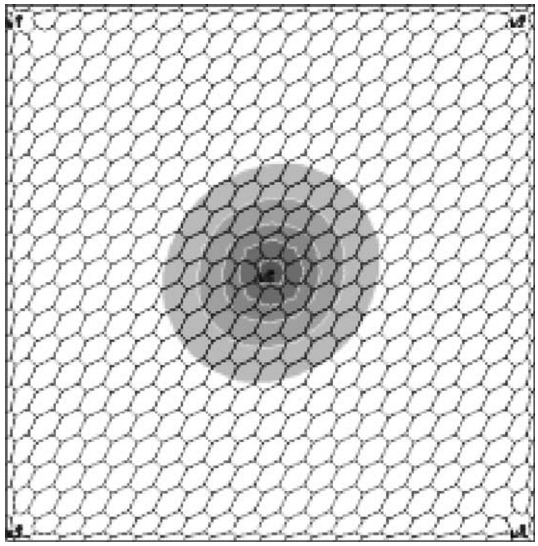

Fig. 11. Saturation for case two calculated by the CVFA.

Table 7
Water break-through times

Method	Gird	Well 1 (day)	Well 2 (day)	Well 3 (day)	Well 4 (day)
CVFA	Case 1	217.0	217.0	217.0	217.0
CVFA	Case 2	380.0	293.0	293.0	380.0
CVFE	Case 1	217.0	217.0	217.0	217.0
CVFE	Case 2	386.5	296.0	296.0	386.5

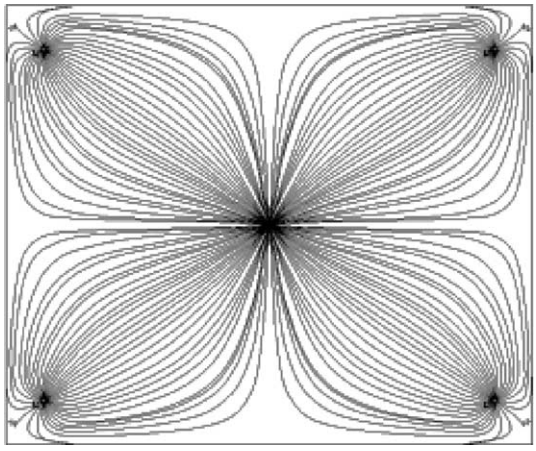

Fig. 12. Streamlines for case one calculated by the CVFA.

wells are the same: 217 days for both the CVFA and CVFE. For case two, the water break-through times of the second and third wells are 87 days and 90.5 days shorter than those of the first and fourth wells by the CVFA and CVFE, respectively. Thus we see that the CVFA is slightly better than the CVFE in reducing the grid orientation effect. The streamlines for case one by the CVFA are illustrated in Fig. 12. From our numerical experiments we have observed that the CVFA can easily generate streamlines, which are very useful in understanding the essentials of oil recovery processes.

4. Concluding remarks

We have introduced a new control volume method. This method is based on function approximations, so we call it the control volume function approximation method. We have studied three function approximations: 'bilinear', spline, and distance weighted. The spline shape functions are the most useful from our numerical experience because the distance weighted approach involves the choice of a power factor and the bilinear approach is valid only for four interpolation nodes. Our numerical tests show that this new method produces smaller approximation errors in the approximation of both the pressure and velocity than the CVFE. The two-phase flow simulation experiments demonstrate that the CVFA is also better in reducing grid orientation effects. The most advantageous feature of the CVFA is that it has no requirement on the shape of elements (see the numerical test II). It is particularly suitable for hybrid grid porous medium simulation, which can correctly describe the features of fluid flow near wells, faults, and irregular boundaries. The treatment of these features by the CVFA is being investigated.

Acknowledgements

The authors would like to thank Dr. Zhongxiao Wang for preparing some of the figures in this paper. Also, the authors wish to thank the referees for many helpful comments and suggestions in this paper. This work is supported in part by National Science Foundation grants DMS-9972147 and INT-9901498.

References

[1] Antontsev SN. On the solvability of boundary value problems for degenerate two-phase porous flow equations. Dinamika Splošnoĭ Sredy Vyp 1972;10:28–53 (in Russian).
[2] Aziz K, Settari A. Petroleum reservoir simulation. London: Applied Science Publishers Ltd; 1979.
[3] Bear J. Dynamics of fluids in porous media. New York: Dover; 1972.
[4] Chavent G, Jaffré J. Mathematical models and finite elements for reservoir simulation. Amsterdam: North-Holland; 1978.
[5] Chen Z. Degenerate two-phase incompressible flow I: existence, uniqueness and regularity of a weak solution. J Differen Equat 2001;171:203–32.
[6] Chen Z. Degenerate two-phase incompressible flow II: regularity, stability and stabilization. J Differen Equat 2002;186:345–76.
[7] Chen Z, Ewing RE. Comparison of various formulations of three-phase flow in porous media. J Comp Phys 1997;132:362–73.
[8] Chen Z, Ewing RE, Shi Z-C (Eds.), Numerical treatment of multiphase flows in porous media, Lecture notes in physics, vol. 552, Springer-Verlag, Heidelberg, 2000.
[9] Chen Z, Huan G, Li B. An improved IMPES method for two-phase flow in porous media. Transp Pororus Media, in press.
[10] Ciarlet PG. The finite element method for elliptic problems. Amsterdam: North-Holland; 1978.
[11] Ewing RE, editor. The mathematics of reservoir simulation. Philadelphia: SIAM; 1983.
[12] Fung LS, Hiebert AD, Nghiem L. Reservoir simulation with a control volume finite element method, SPE 21224, the 11th SPE Symposium on Reservoir Simulation, Anaheim, February 17–20, 1991.
[13] Heinrich B. Finite difference methods on irregular networks. Basel: Birkhauser; 1987.
[14] Peaceman DW. Fundamentals of numerical reservoir simulation. New York: Elsevier; 1977.
[15] Peaceman DW. Interpretation of well-block pressures in numerical reservoir simulation, SPE 6893, 52nd Annual Fall Technical Conference and Exhibition, Denver, 1977.
[16] Schumaker LL. Spline functions: basic theory. New York: Wiley; 1981.
[17] Verma S, Aziz KA. Control volume scheme for flexible grids in reservoir simulation, Paper SPE37999, the 1997 SPE Symposium on Reservoir Simulation, Dallas, June 8–11, 1997.